Magnetic circular dichroism in core-level x-ray photoelectron spectroscopy of altermagnetic RuO_2 films

Y. Lytvynenko,[1,2] A. Akashdeep,[1] T. P. Vo,[3,4] O. Tkach,[1,5] S. V. Chernov,[6] A. Gloskovskii,[6] C. Schlueter,[6] C. Luo,[7] V. Ukleev,[7] F. Radu,[7] F. Kronast,[7] T. Hiroto,[8] A. Winkelmann,[9] J. Minár,[3] M. Kläui,[1] G. Schönhense,[1] G. Jakob,[1] H. J. Elmers,[1,*] and O. Fedchenko[1,10]

[1]*Institut für Physik, Johannes Gutenberg-Universität, Staudingerweg 7, D-55128 Mainz, Germany*
[2]*Institute of Magnetism of the NAS and MES of Ukraine, 03142 Kyiv, Ukraine*
[3]*University of West Bohemia, New Technologies Research Center, Plzen 30100, Czech Republic*
[4]*Institute of Physics, Czech Academy of Sciences, Praha 6, Czech Republic*
[5]*Sumy State University, Rymski-Korsakov 2, 40007 Sumy, Ukraine*
[6]*Deutsches Elektronen-Synchrotron DESY, 22607 Hamburg, Germany*
[7]*Helmholtz-Zentrum Berlin für Materialien und Energie, Albert-Einstein Str. 15, 12489 Berlin, Germany*
[8]*Nara Institute of Science and Technology, Takayamacho 5, 630-0192 Nara, Japan*
[9]*Academic Centre for Materials and Nanotechnology, AGH University of Science and Technology, 30059 Kraków, Poland*
[10]*Physikalisches Institut, Goethe Universität Frankfurt, Max-von-Laue-Strasse 1, 60438 Frankfurt am Main, Germany*

(Received 7 June 2025; revised 6 November 2025; accepted 16 December 2025; published 5 January 2026)

While ferromagnetism and antiferromagnetism are well-established classes of magnetic order, a third class of collinear magnetic order, termed altermagnetism, has recently attracted scientific interest. We measured magnetic circular dichroism (MCD) in core-level photoemission (XPS) at the Ru $2p_{3/2}$ and $2p_{1/2}$ core levels in epitaxial $RuO_2(110)/TiO_2(110)$ films using circularly polarized x rays at 6 keV, as well as x-ray magnetic circular dichroism (XMCD) in resonant x-ray absorption at the Ru $M_{3,2}$ ($3p_{3/2}$ and $3p_{1/2}$) edges. Charge transfer multiplet calculations show that the MCD-XPS and the XMCD can be explained by an altermagnetic locking of Ru magnetic moments and a distorted crystal field orientation. The distortion is caused by the epitaxial strain. The collinear magnetic moments in RuO_2 occupy sublattice sites with distorted octahedral crystal fields that are rotated by 90° with respect to each other. A change in the sign of the MCD-XPS at different sample positions indicates the presence of altermagnetic domains with the size of around hundreds of micrometers.

DOI: 10.1103/x2h4-rtky

I. INTRODUCTION

The two elementary classes of crystals with collinear magnetic order—ferromagnetic and antiferromagnetic—have applications in the field of spintronics [1–7]. The spin polarization of ferromagnetic conduction bands breaks time-reversal symmetry, leading to spin-polarized currents in spintronic devices. In antiferromagnetic crystals, time reversal with lattice translation restores the spin symmetry, resulting in Kramer's degeneracy and the cancellation of all first-order magnetic circular dichroism (MCD) effects. Nevertheless, antiferromagnetic materials have recently attracted scientific interest due to their potential for exploiting intrinsic spin-orbit torques [6,8,9]. Unlike ferromagnets, their compensated magnetic moments avoid stray field interaction and enable faster switching thanks to their similarly compensated angular momentum [9–11].

Following an early prediction of spin-polarized conduction electrons in MnTe [12], a third class of collinear magnetic order, called altermagnetic, has been predicted [13,14] and confirmed spectroscopically [15–17]. In altermagnets, the symmetry is given by a combination of time reversal in spin space combined with a rotation in real space instead of a translation. Consequently, spin-polarized conduction bands are permitted despite the presence of compensated magnetic moments. The combination of advantages of ferromagnetic and antiferromagnetic properties could enable a wide range of technological applications. Altermagnets could be particularly useful in spintronics, a field in which signals are carried by the spins of quasiparticles rather than charge.

Ab initio calculations have predicted the presence of time-reversal symmetry-breaking MCD in altermagnets across the entire spectral range, including x rays [18–20]. This phenomenon has recently been used to visualize the altermagnetic band structure in RuO_2 [15].

Although rutile RuO_2 was among the first materials for which altermagnetism, related to spin-dependent transport properties, was discussed [21–33], its magnetic ground state has recently been debated. While neutron diffraction [34], transport measurements [35,36], x-ray scattering [37], and spin- and angle-resolved photoemission spectroscopy [38] revealed altermagnetism in RuO_2, recent *ab initio* theory [39] and experiments [40–48] have called into question the magnetic order in particular of bulk RuO_2. Theoretical studies suggest that the onset of altermagnetism in epitaxial RuO_2 films could occur near a quantum critical transition, whereby oxygen deficiencies, symmetry breaking at the interfaces, or epitaxial strain [39,49–51] would stabilize the magnetic order. Indeed, recent experimental data on thin films

*Contact author: elmers@uni-mainz.de

seems to support the occurrence of altermagnetism in RuO_2 [15,52–57].

We measured the magnetic circular dichroism in the soft and hard x-ray ranges. MCD has previously been used successfully in the study of ferromagnetic materials [58–66]. Since the photon operator acts exclusively on orbital states, MCD in collinear magnets requires the combination of exchange spin splitting and spin-orbit interaction [67–69]. With the exception of resonant x-ray absorption [70,71], even in ferromagnets, MCD is typically quite weak because, for core-level excitation, the exchange splitting is small. For valence band excitations, the relativistic spin splitting is small, too [58]. However, for the antiferromagnetic order, which has combined time-reversal and parity/translation symmetry, MCD and other time-reversal symmetry-breaking linear responses are absent [14].

We previously established the key signature of the altermagnetic phase in epitaxial RuO_2 films using MCD in valence band photoemission spectroscopy [15]. Here, we demonstrate that a substantial MCD is evident at the Ru $2p$ core-level x-ray photoemission spectra and x-ray absorption at the Ru $M_{3,2}$ edges in epitaxial $RuO_2(110)/TiO_2(110)$ films. This elucidates the role of epitaxial strain in these films. We have performed charge transfer multiplet calculations [72,73] to trace the MCD back to the locking of Ru magnetic moments and the local crystal field orientation at the Ru^{4+} ions, considering the strain-induced distortions of the crystal field. The MCD could be useful in investigating the structure of altermagnetic domains.

II. EXPERIMENT

The rutile crystal structure of metallic RuO_2 has a collinear, compensated magnetic order [34,37]. The alternating orientation of the distorted octahedral crystal fields at Ru^{4+} ions enables the occurrence of altermagnetism [13,74]. It is predicted that this rutile crystal family will exhibit topological properties as well [75].

We have grown epitaxial $RuO_2(110)$ films with a thickness of 7 nm to 34 nm by pulsed laser deposition on $TiO_2(110)$ substrates that were heated to 400 °C during deposition. The oxygen pressure used was 0.02 mbar and typical growth rates were 1.9 nm/min with the KrF excimer laser operating at 10 Hz and 150 mJ pulse energy. The film thicknesses were determined from x-ray reflectometry (XRR) at grazing incidence. In addition, XRR indicates that all samples have a surface roughness of less than 0.3 nm. Φ scans reveal the epitaxial relation between substrate and film. They show a twofold symmetry of (200) peaks aligned with that from the substrate. The peak width in Φ is 2°. The widths of the out-of-plane scattering peaks in 2Θ indicate a coherent scattering size that increase from $D = 7$ nm for the 7-nm-thick film to $D = 30$ nm for the 32.5-nm-thick film, respectively.

For the 7-nm-thick film, the x-ray diffraction data shown in Fig. 1(a) reveal a lattice spacing between the (110) planes of $d = 3.23$ Å when measuring the scattering vector normal to the (110)-oriented rutile TiO_2 substrate. Assuming an angle of 90° between the a and b axes, d results in a lattice constant $a = 4.56$ Å. This corresponds to a 0.57% expansion with respect to the bulk RuO_2 value ($a = 4.543$ Å). Note that the pseudomorphic growth mode suggested in Refs. [36,76] requires a 2.3% expansion (TiO_2 lattice constant $a = 4.653$ Å) of the in-plane lattice spacing in the ab plane, i.e., between the $(1-10)$ planes. Explaining the spacing between the (110) and $(1-10)$ planes simultaneously necessitates a deviating angle of 90.7° between the a and b axes. Fitting a Laue oscillation model to the oscillations observed to the left and right of the main peak in Fig. 1(a) results in a thickness of 6.1 nm, which is reasonably consistent with the thickness of 7 nm obtained from the x-ray reflectometry (XRR) data at grazing incidence. Figure 1(b) shows the reflection high-energy electron diffraction (RHEED) pattern of the 7-nm-thick $TiO_2(110)/RuO_2(110)$ film, obtained with the electron beam aligned along the $TiO_2[001]$ direction. The diffraction pattern indicates that the single crystalline film is well aligned with the substrate and has a very low roughness. The presence of the RHEED pattern indicates that the film is crystalline at the surface. Figure 1(c) shows the x-ray reflectivity data. From the fit values for the thickness (7.1 nm), for the roughness (0.34 nm), and for the density (7.43 g/cm^3) were extracted.

X-ray diffraction experiments were also conducted for thicker films. A 17-nm- and a 32.5-nm-thick film show a (110) lattice spacing of $d = 3.20$ Å and $d = 3.18$ Å, respectively. A determination of the lattice constant c from higher order x-ray reflexes was only possible for the 32.5-nm-thick film, resulting in a compressive strain of -1.4% with respect to the RuO_2 bulk value.

In the following discussion of MCD spectroscopy, we focus on the 7-nm-thick film. This sample was capped *in situ* with a 2-nm-thick Al film using magnetron sputtering at room temperature. The presence of Laue oscillations in the XRD data [Fig. 1(a)] indicates that the film has sharp interfaces. Previous results also revealed that the capping does not modify the underlying film [77], as confirmed by the x-ray absorption and x-ray photoelectron spectroscopy, which show a unique Ru^{4+} ionic state. Additional structural and XMCD results for a 32.5-nm-thick film can be found in the Supplemental Material [78].

The samples exhibit no discernible remanent magnetization, consistent with prior SQUID magnetometry studies of comparable RuO_2/TiO_2 thin films [76]. The upper limit of the net remnant magnetization is estimated at 0.001 μ_B per Ru atom.

Photoelectrons were excited by circularly polarized hard x rays at an angle of incidence of 10° (beamline P22, PETRA III, DESY, Hamburg) and recorded using the time-of-flight momentum microscope [79,80]. Circular polarization was formed using a diamond phase retarder acting as a $\lambda/4$ plate. At 6 keV, circular polarization is obtained with a 400-μm-thick (100) diamond phase plate at a glancing angle of 84.8°, where the quarter-wave condition corresponds to an angular offset of 93 in. from the Bragg position. Independent reference measurements revealed a degree of polarization of >99.8%. The photon bandwidth is set to 500 meV and the sample temperature used is 30 K. The azimuthal orientation of the sample [see Fig. 2(a)] has been adjusted so that the photon incidence plane coincides with the easy spin axis of RuO_2, i.e., the [001] c axis [34,76,81]. The lattice structure is sketched in Figs. 2(b) and 2(c).

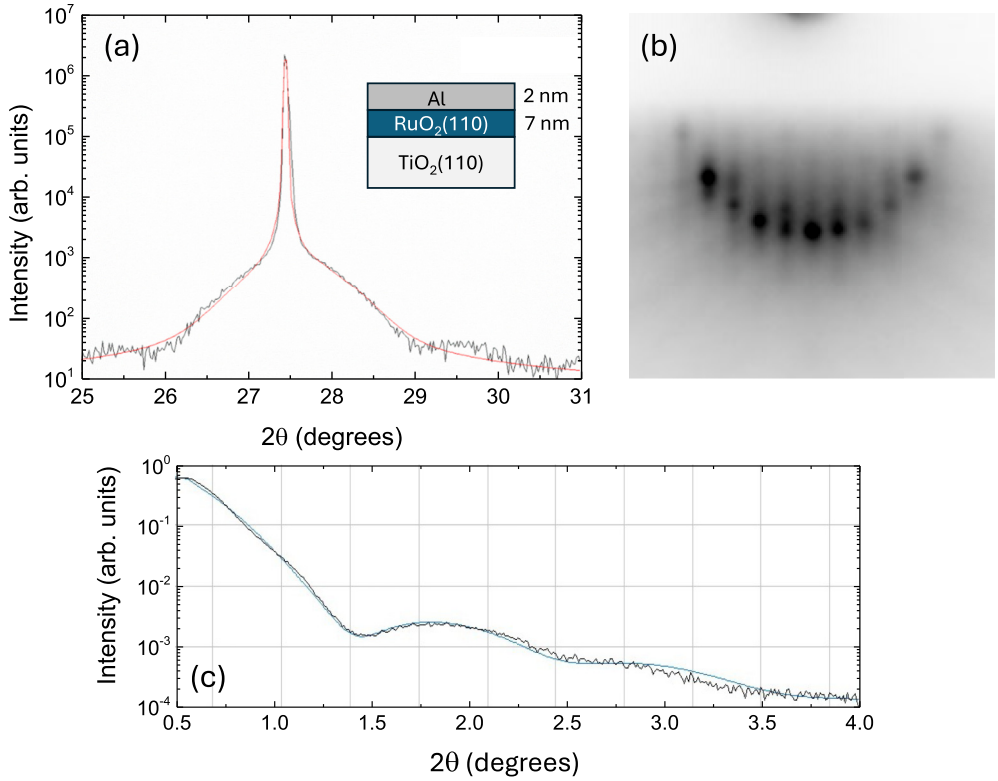

FIG. 1. Structural and surface characterization of $TiO_2(110)/RuO_2(110)$ films. (a) XRD intensity as a function of 2Θ measured with the scattering vector normal to the (110)-oriented rutile substrate for the 7-nm-thick film. The black line represents the experimental data and the red line is a two-peak fit to the sharp substrate peak and the broader RuO_2 peak. (b) RHEED pattern (before Al capping) for the same sample, with the electron beam aligned along $TiO_2[001]$. (c) X-ray reflectivity shown as intensity versus 2Θ for the same sample. The black line represents the experimental data; the full blue line is a fit resulting in a thickness of 7.1 nm.

The XMCD spectroscopy measurements were performed using the VEKMAG end station [82] at BESSY II, Helmholtz Zentrum Berlin (HZB), Germany, during the multibunch operational mode of the synchrotron storage ring. The x-ray absorption spectra (XAS) were measured at 6 K for x-ray energies in the vicinity of the $M_{3,2}$ absorption edges of Ru in a zero magnetic field. The photocurrent was normalized to the current of a Ta-mesh monitor located in the x-ray beam path in order to compensate for variations in the ring current and in the transmission function of the optical elements. The XMCD spectra were obtained by subtracting the intensity between the XAS spectra measured for right- and left-circular x-ray polarizations with a degree of polarization of 77%.

III. RESULTS

In order to characterize the structural properties of the sample volume under investigation, x-ray photoelectron diffraction (XPD) was performed at the Ru $2p$ core levels. Figure 2(d) shows the XPD pattern measured at the Ru $2p_{3/2}$ level. Prominent sets of parallel Kikuchi lines occur at $k_{x,y} = \pm 2$ Å^{-1}. An additional pair of horizontal Kikuchi lines is visible at $k_y = \pm 1$ Å^{-1} indicating the (110) orientation and the rectangular unit cell of the epitaxial film. The sharpness of the XPD pattern is insufficient to determine the epitaxial strain. Meanwhile, the in-plane strain caused by the lattice mismatch between the TiO_2 substrate and the pseudomorphic growth of RuO_2 has been confirmed by x-ray diffraction [15].

Figure 2(e) shows the calculated XPD pattern obtained using the Bloch wave approach described in Refs. [83,84]. While this method captures the low-intensity (dark) Kikuchi lines visible in the experimental data quite well, the distribution of high-intensity (white) areas differs.

The XPD pattern calculated using multiple-scattering theory and the fully relativistic one-step photoemission model [85] captures both features, the low-intensity Kikuchi lines and the high-intensity areas of the experimental data, very well. The good agreement between the calculated and experimental patterns, as shown in Fig. 2(e), confirms the structural quality of the probed sample volume.

Figure 3 shows typical experimental results for the XPS spectra, measured at $h\nu = 6000$ eV. The photoelectron intensity was averaged over a parallel momentum circle with a diameter of 7 Å^{-1} centered on the surface normal, corresponding to a polar angle range of 0–5°.

The small differences in the incident x rays for opposite helicities were accounted for by normalizing the measured photoelectron intensities to reference spectra of the Si $2p$ peak of a pure silicon crystal, which were measured in the same configuration. These reference measurements also confirmed the absence of any shifts in photon energy between right- and left-circularly polarized x rays.

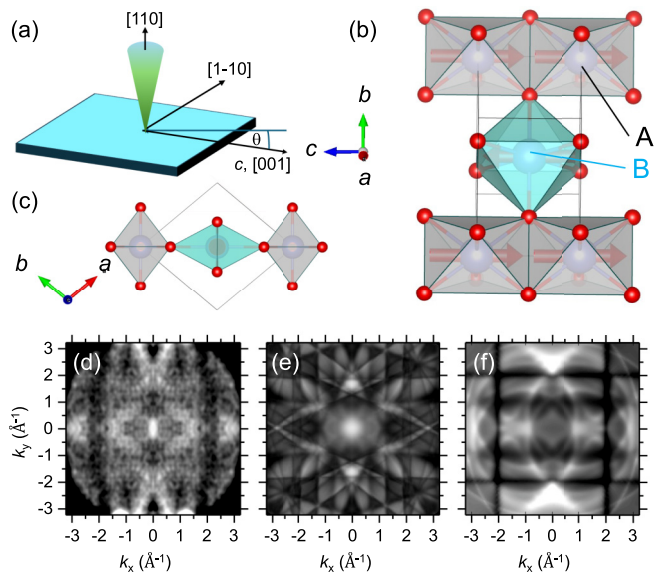

FIG. 2. (a) Sketch of the experimental geometry. (b) A RuO_2(110) layer highlighting the octahedral crystal field of a bulk single crystal of RuO_2 formed by the oxygen ions (red) around a Ru ion (blue). The two inequivalent sublattices are labeled A and B. (c) An epitaxial RuO_2(110) layer viewed along the c axis, indicating tensile epitaxial strain in the [1 − 10] direction. The strain in the sketch is exaggerated for clarity. (d) Experimental x-ray photoelectron diffraction (XPD) at the Ru $2p_{3/2}$ core level excited at 6 keV. (e) A calculated XPD pattern using the Bloch wave approach. (f) A calculated XPD pattern using multiple-scattering theory and the fully relativistic one-step photoemission model.

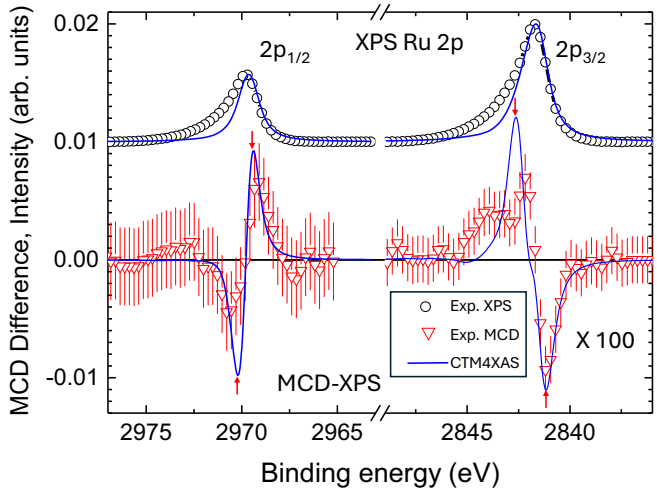

FIG. 3. Top: Ru $2p_{3/2}$ and $2p_{1/2}$ XPS spectra at a photon energy of 6 keV (open circles), averaged over circularly polarized x rays of both helicities. The averaged spectra are normalized to the maximum, divided by a factor of 100 and shifted by 0.01 for better visibility. Bottom: the MCD difference ($I^+ - I^-$) of the spectra measured with opposite helicity is shown as open triangles. The full lines represent the results obtained by charge transfer multiplet calculations using the approach of Refs. [72,73]. The appearing minus-plus and plus-minus features are indicated by arrows.

The top part of Fig. 3 shows the total intensity curve in the region of the spin-orbit split $2p$ lines of ruthenium, averaged over the two helicities of the x rays. The lower part of Fig. 3 shows the difference in the partial intensities. As the binding energy increases, a plus-minus feature appears at the $2p_{3/2}$ peak and a weaker, broader minus-plus feature appears at the $2p_{1/2}$ peak.

The plus-minus features correspond to a peak shift of the I^+ peaks with respect to the I^- peaks. These peak shifts occur in opposite directions for the $2p_{3/2}$ and $2p_{1/2}$ peaks of the two components of the $2p$ spin-orbit doublet. The observed differences correspond to peak shifts of 0.1 eV.

The main result of this experiment is that the XPS spectra reveal a finite difference when exciting with either circularly right- or left-polarized light, which is similar to that observed in ferromagnetism. Therefore, we attribute this effect to a magnetic circular dichroism. This finding directly confirms the time-reversal symmetry breaking in the altermagnetic RuO_2 films. Strictly speaking, circular polarization only tests the mirror symmetry of the experimental setup when photon momentum is disregarded. It does not test time-reversal symmetry. If the setup is symmetric, as in our case, an asymmetry could be caused by a chiral crystal structure or a magnetic origin. However, a chiral crystal structure has never been reported for either RuO_2 or the substrate material, TiO_2. Therefore, we do not consider a chiral structure to be the origin of the observed asymmetry. In our opinion, the magnetic origin, which is time-reversal asymmetric, is the most plausible explanation.

The microscopic origin of the magnetic circular dichroism in altermagnets starts from a similar picture to that in ferromagnets [86]. In this model, the emission from the two magnetic sublattices with opposite magnetizations is considered separately. Excitation of electrons from the spin-orbit split $2p_{3/2}$ and $2p_{1/2}$ core levels into free electron states by right-circularly polarized light leads to preferential emission of up electrons from the $2p_{3/2}$ level and down electrons from the $2p_{1/2}$ level, due to the spin-orbit interaction. Assuming free-electron final states is justified since the kinetic energy is approximately 3 keV above the Fermi level. X rays with reversed helicity excite electrons with opposite spins. In both cases, the emitted intensity is exactly the same, but the emitted electrons are spin polarized along the photon spin orientation.

The exchange splitting, which is caused by the intra-atomic exchange interaction between the conduction band and the core level, is much smaller than the spin-orbit splitting. Thus the two $2p$ states are split further with respect to the total angular momentum component m_j. Consequently, circularly polarized x rays of positive helicity will preferentially excite spin-up electrons from the $2p_{1/2}$ state and spin-down electrons from the $2p_{3/2}$ state. The essential condition is that the spin orientation of the sample must be aligned with the photon spin. Reversing the helicity reverses the spin orientation; however, due to the exchange splitting, the energetic positions of the spin-down and spin-up electrons in the emission spectrum are swapped. The difference between the two spectra for opposite helicity exhibits the plus-minus and minus-plus features, respectively [86], as indicated by the arrows in Fig. 3.

The same dichroism profile, but with an opposite sign, is obtained when the magnetization is reversed. Therefore,

TABLE I. Parameters used for the simulation of XAS and XPS spectra given in eV. The crystal field parameters $10Dq$, Ds, and Dt are adapted to the experimental spectra. The Slater integrals (SI) correspond to 80% of the Hartree-Fock values. The spin-orbit interaction SO is given by the atomic value. For simulating the XPS spectra the additional Hubbard parameters Δ, U_{pd}, U_{dd}, T_{eg}, and T_{2g} are used.

XAS/XPS	$10Dq$	Ds	Dt	SI	SO
	2.96	±0.06	±0.10	80% HF	0.15
XPS	Δ	U_{pd}	U_{dd}	T_{eg}	T_{2g}
	6	3	2	2.0	1.0

one would expect the difference spectra of the two magnetic sublattices to cancel each other out. However, in the altermagnetic compound RuO_2, the orientation of the sublattice magnetization is locked to the orientation of the crystal field of distorted octahedral crystal field [see Fig. 2(b)]. In bulk RuO_2, a rotation around the c axis by 90° combined with time reversal restores the original relationship between the crystal field and the spin direction. Since time reversal also swaps the helicity of the circularly polarized x rays, the MCD-XPS effect is not permitted. In contrast, the epitaxial growth of $RuO_2/TiO_2(110)$ films causes tensile epitaxial strain along the [1 − 10] direction and compressive strain along the [001] direction, similar to that observed in Ref. [87]. Consequently, the rotational symmetry around the c axis is slightly distorted as shown qualitatively in Fig. 2(c). The octahedral crystal field of sublattice B is stretched along its long axis, whereas the octahedral field of sublattice A is compressed.

This distorted crystal field further alters the spectra due to the direct interaction of the initial and final state levels within the crystal field, as well as due to correlation effects described by atomic multiplet theory. As the crystal field differs between the two sublattices, complete compensation of the difference spectra is not achieved, resulting in residual altermagnetic circular dichroism.

To further confirm this model, we performed charge transfer multiplet calculations using the approach described in Refs. [72,73], in which the crystal fields were described empirically using the crystal field parameters $10Dq = 2.96$, $Ds = 0.06$, and $Dt = 0.1$ (numbers are in eV) for a distorted octahedral symmetry. Additional parameters describe the Slater integrals SI, which were assumed to correspond to 80% of the Hartree-Fock values [88,89], spin-orbit interaction SO of 0.15 eV, charge transfer energy ($\Delta = 6$), Hubbard parameters ($U_{pd} = 3$, $U_{dd} = 2$), and hopping integrals ($T_{eg} = 2.0$, $T_{2g} = 1.0$), as suggested in Refs. [73,90,91]. (See Table I.)

The main crystal field parameter, which splits the Ru $4d$ orbitals with e_g and t_{2g} symmetry, is set to $10Dq = 2.96$ following previous work [92,93]. The boundary condition $Ds = (5/3)Dt$ further sets the energies of the occupied low energy $4d$ orbitals with d_{xy} and $d_{zx,zy}$ symmetries to equal values in order to define the local magnetic moment. The difference in crystal fields between the two magnetic sublattices, which correspond to strained and squeezed octahedra, is modeled by $Dt > 0$ and $Dt < 0$. The calculated MCD of the contributions

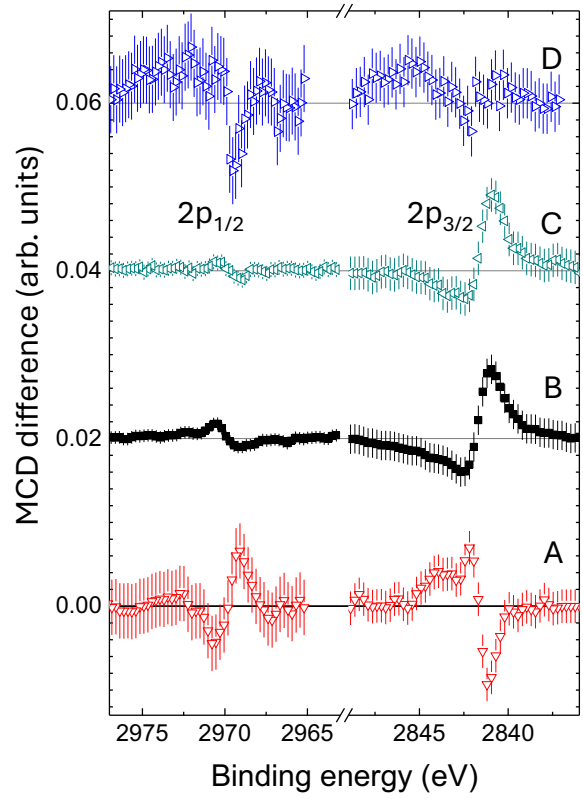

FIG. 4. MCD difference spectra ($I^+ - I^-$) for the Ru $2p_{3/2}$ and $2p_{1/2}$ signals, which were measured at different positions on the sample. The scale is identical to Fig. 3.

of the two magnetic sublattices with opposite signs increases with increasing octahedral field distortion Dt. The total calculated MCD-XPS asymmetry varies little for Dt in the range 0.03–0.09, but increases steeply for larger values of Dt. The asymmetry calculated for $Dt = 0.06$ corresponds well with our experimental data. This value corresponds to 2% of the $10Dq$ value, which determines the significant splitting of the e_g and t_{2g} orbitals. Given the epitaxial strain, this value seems reasonable. Note that the charge transfer energy Δ and the Hubbard parameters cause a shift in binding energy but do not singificantly change the spectra.

Assuming lifetime broadening (modeled by a Lorentzian function) of 0.5 eV, a value of $Dt = 0.06$ results in a difference similar to that observed experimentally. The calculated spectra are in good agreement with the experimental spectra. However, the exchange splitting of the initial state is much smaller than the lifetime broadening, meaning no further spectral details can be resolved.

Figure 4 shows the measured MCD spectra at selected positions on the sample, separated by several hundred micrometers. The footprint of the incident x rays is an ellipse with a diameter of 10 × 15 μm. Both signs of the MCD signal are observed (see spectra A and B in Fig. 4), indicating the presence of altermagnetic domains with opposite directions of the Néel vector. At some positions, we observe an almost vanishing MCD signal (see spectrum D in Fig. 4), which we tentatively attribute to the presence of multiple domains and domain walls within the probed region.

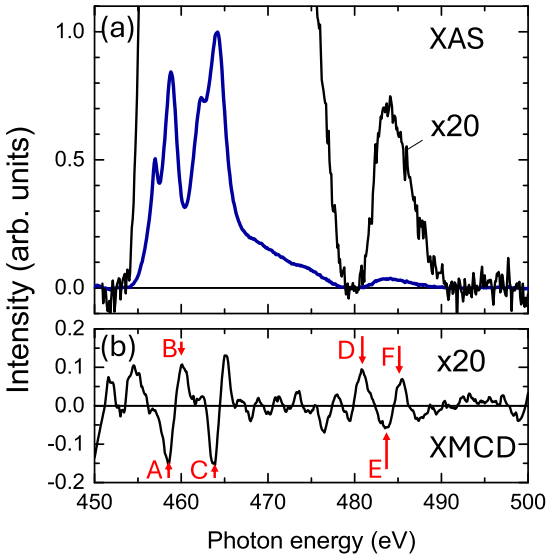

FIG. 5. (a) X-ray absorption spectrum within the energy range of the Ru $M_{3,2}$ edges, averaged for right- and left-circularly polarized x-ray light. The peak at 485 eV corresponds to the Ru M_2 edge, which is smaller by a factor of 20 due to the smaller cross section of the M edges. The large peaks between 455 and 465 eV correspond to the Ti L-edge peaks of the underlying substrate, which overlap with the Ru M_3 absorption edge. (b) The XMCD spectrum was calculated from the difference in the x-ray absorption spectra measured for opposite x-ray helicities. Arrows indicate the prominent minus-plus-minus and plus-minus-plus features at the positions of the Ru $M_{3,2}$ edges.

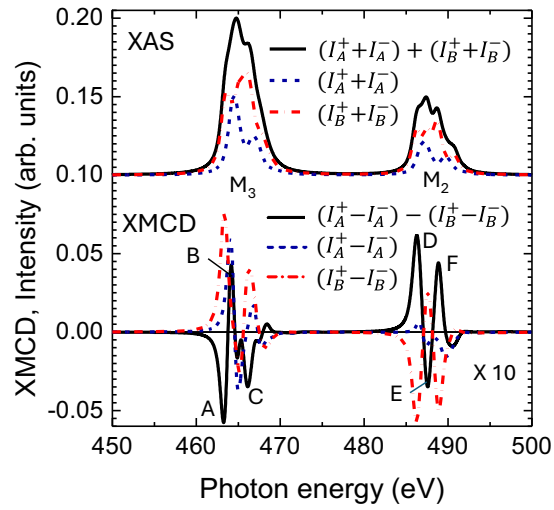

FIG. 6. Ru $M_{3,2}$ edge x-ray absorption spectra calculated using charge transfer multiplet calculations [72,73] with the same correlation and crystal field parameters as in the case of the XPS spectra shown in Fig. 3. The calculated sum and difference spectra of the calculated intensities for opposite x-ray helicities I_i^+ and I_i^- and sublattices $i = A, B$ are shown as dashed and full lines, respectively. The full lines indicate the expected total XAS and XMCD spectra for altermagnetic RuO_2.

While the effect of different crystal fields on the XPS spectra is comparatively small, resulting in magnetic circular dichroism close to the detection limit after summation of the signal from two sublattices with opposite magnetization, larger dichroism effects can be expected for resonant x-ray absorption, where the final states are spin-polarized valence states.

Figure 5 shows the experimental data for the x-ray absorption (XAS) and x-ray magnetic circular dichroism (XMCD) spectra of 7-nm-thick epitaxial RuO_2 films, which were measured using a geometry similar to that used for the MCD-XPS spectra. The large peaks between 455 eV and 465 eV are the Ti L-edge peaks from the substrate, which overlay the Ru M_3 absorption edge at 460 eV. The peak at 485 eV corresponds to the Ru M_2 edge, which is smaller by a factor of 20 due to the smaller cross section of the M edges.

The difference (XMCD) spectra shown in Fig. 5(b) have been smoothed using a digital Sawatzky-Golay filter with an energy interval of 2.5 eV (25 data points). The Ru M_2 edge, which is not obscured by the Ti signal, exhibits a plus-minus-plus structure (D, E, and F, indicated by the red arrows). The maxima of this XMCD signal reach values of ±10% of the Ru M_2 edge absorption maximum. A similar-sized minus-plus-minus feature (A, B, and C) can be identified in the energy region of the Ru M_3 edge at 460 eV. Due to the strong overlying signal from the Ti L_3 edge, there may also be an overlying XMCD signal. However, as TiO_2 is known to be diamagnetic and lacks occupied d-electron orbitals, we assume that the XMCD signal is not caused by the Ti ions. Therefore, the XMCD of the superimposed Ru M_3 edge is still visible.

In the representation shown in Fig. 5(a) the energy-independent background signal has been subtracted. Therefore, the total measured XMCD asymmetry, calculated by dividing the XMCD by the total intensity including the background signal, is significantly smaller than Fig. 5 suggests. The XMCD maxima at both Ru M edges then correspond to a maximum asymmetry of 5×10^{-3}. An even smaller XMCD asymmetry of 1×10^{-3} was observed for a 32.5-nm-thick film (see the Supplemental Material [78]).

In principle, sum rule analysis of the measured XMCD spectra could yield distinct values for the spin and orbital moments. However, it is not possible to uniquely separate the contributions from opposite sublattices and the total XMCD spectra result in zero magnetic moments within error limits.

The corresponding calculated spectra are shown in Fig. 6. The phenomenological crystal field parameters are identical with the parameters used for the MCD-XPS simulation shown in Fig. 3. We did not allow charge transfer for this multiplet calculation to restrict the initial state to $4d^4$. The fact that in $2p$ XAS the electron is excited to a $4d$ state implies that the $2p$ XAS process is self-screened and therefore a simplified description without charge transfer is justified. The x-ray absorption spectra differ for the two sublattices, which have different crystal field parameters $Dt = \pm 0.06$, $I_{\mathrm{XAS,A}} = I_A^+ + I_A^-$, and $I_{\mathrm{XAS,B}} = I_B^+ + I_B^-$. Similarly, the x-ray magnetic circular dichroism spectra differ: $I_{\mathrm{XMCD,A}} = I_A^+ - I_A^-$ and $I_{\mathrm{XMCD,B}} = I_B^+ - I_B^-$. Due to the opposite orientation of the magnetic moments in sublattices A and B, the corresponding XMCD spectra have the opposite signs. Consequently, the total XMCD signal, resulting from $I_{\mathrm{XMCD,A}} - I_{\mathrm{XMCD,B}}$, is not fully compensated, unlike the sublattice magnetization.

Sublattice A shows a positive maximum at the rising M_3 edge (Fig. 6). In this calculation, sublattice B also exhibits a positive maximum at the rising edge; however, considering the opposite direction of the magnetic moment, the spectrum reverses its sign. As these two maxima occur at different photon energies, they do not cancel out.

The total XMCD signal calculated from both sublattices exhibits minus-plus-minus (A, B, and C) and plus-minus-plus (D, E, and F) features at the M_3 and M_2 edges, respectively, which are in good agreement with the features observed experimentally. The order of magnitude of the calculated XMCD signals also agrees with the observed XMCD maxima, which means that the assumed strain factor is realistic.

The magnetic moments calculated from the theoretical simulation using sum rule analysis are $-1.44\,\mu_B$ at site A and $+1.85\,\mu_B$ at site B; orbital magnetic moments are negligible. Consequently, the theoretical system does not describe compensated magnetic order, but rather ferrimagnetic order. This discrepancy with the experimental system may be due to the ionic model, combined with crystal fields, only poorly describing the actual electronic states. Nevertheless, we believe it is valuable to present the results of this simple modeling, as it provides a useful phenomenological insight into the underlying processes.

IV. SUMMARY

Observing magnetic circular dichroism both in Ru $2p$ core-level photoemission and in photoabsorption of the Ru $M_{3,2}$ edges confirms the presence of magnetic order with time-reversal symmetry breaking in thin epitaxial $RuO_2(110)/TiO_2(110)$ films. The Néel vector lies in the in-plane [001] direction. In this geometry, XMCD is forbidden in undistorted RuO_2 when the Néel vector lies strictly along the c axis [19,94]. However, it has been demonstrated that XMCD is permitted when the Néel vector has a finite projection onto the ab plane. For instance, a canted Néel vector from the c axis towards the [110] out-of-plane direction in combination with a finite angle of incidence θ allows for a finite XMCD in nonstrained bulk RuO_2. We cannot exclude this possibility. Nevertheless, previous experimental reports [37,54] suggest a Néel vector orientation that is parallel to the c axis. Therefore, we searched for an alternative explanation. Charge transfer multiplet calculations suggest that magnetic circular dichroism originates from the distortion of the octahedral crystal field at the Ru ions. The close correlation between the calculated and experimental spectra indicates that the crystal distortion caused by epitaxial strain is responsible for the observed magnetic circular dichroism effects in both the x-ray absorption and in the x-ray photoelectron spectra. Strictly speaking, epitaxial strain leads to inequivalent magnetic sublattices, breaking the rotational symmetry that is usually associated with altermagnetic order when combined with time-reversal symmetry. Since in our system the sublattice magnetization remains fully compensated and Kramer's degeneracy is lifted leading to spin-split bands, we observe altermagnetic order enabled by the strain in RuO_2 thin films.

ACKNOWLEDGMENTS

This work was funded by the Deutsche Forschungsgemeinschaft (DFG) Grants No. TRR 173 268565370 (Projects No. A01, No. A02, and No. B02) and No. TRR 288 422213477 (Project No. B04), by the BMBF (Projects No. 05K22UM1 and No. 05K22UM4), by the EU FET Open RIA Grant No. 766566, and by the Grant Agency of the Czech Republic Grant No. 19-28375X and the Horizon Europe FET Open RIA Grant No. 101070287 (SWAN-on-chip). J.M. and T.P.V. would like to thank the project Quantum Materials for applications in sustainable technologies (QM4ST), funded as Project No. CZ.02.01.01/00/22.008/0004572 by Program Johannes Amos Commenius, called Excellent Research. In addition, T.P.V. acknowledges the Czech Science Foundation Grant No. GA CR 23-04746S. We acknowledge financial support for the VEKMAG project and for the PM2-VEKMAG beamline by the German Federal Ministry for Education and Research (BMBF Projects No. 05K10PC2, No. 05K10WR1, and No. 05K10KE1) and by HZB.

DATA AVAILABILITY

The data that support the findings of this article are not publicly available upon publication because it is not technically feasible and/or the cost of preparing, depositing, and hosting the data would be prohibitive within the terms of this research project. The data are available from the authors upon reasonable request.

[1] A. Freeman and S. D. Bader, Editorial, J. Magn. Magn. Mater. **200**, xi (1999).
[2] C. Chappert, A. Fert, and F. N. Van Dau, The emergence of spin electronics in data storage, Nat. Mater. **6**, 813 (2007).
[3] D. C. Ralph and M. D. Stiles, Spin transfer torques, J. Magn. Magn. Mater. **320**, 1190 (2008).
[4] S. D. Bader and S. Parkin, Spintronics, Annu. Rev. Condens. Matter Phys. **1**, 71 (2010).
[5] S. Bhatti, R. Sbiaa, A. Hirohata, H. Ohno, S. Fukami, and S. Piramanayagam, Spintronics based random access memory: A review, Mater. Today **20**, 530 (2017).
[6] T. Jungwirth, X. Marti, P. Wadley, and J. Wunderlich, Antiferromagnetic spintronics, Nat. Nanotechnol. **11**, 231 (2016).
[7] A. Manchon, J. Železný, I. M. Miron, T. Jungwirth, J. Sinova, A. Thiaville, K. Garello, and P. Gambardella, Current-induced spin-orbit torques in ferromagnetic and antiferromagnetic systems, Rev. Mod. Phys. **91**, 035004 (2019).
[8] O. Gomonay, T. Jungwirth, and J. Sinova, Concepts of antiferromagnetic spintronics, Phys. Status Solidi RRL **11**, 1700022 (2017).
[9] V. Baltz, A. Manchon, M. Tsoi, T. Moriyama, T. Ono, and Y. Tserkovnyak, Antiferromagnetic spintronics, Rev. Mod. Phys. **90**, 015005 (2018).
[10] T. Jungwirth, J. Sinova, A. Manchon, X. Marti, J. Wunderlich, and C. Felser, The multiple directions of antiferromagnetic spintronics, Nat. Phys. **14**, 200 (2018).

[11] A. V. Kimel and M. Li, Writing magnetic memory with ultrashort light pulses, Nat. Rev. Mater. **4**, 189 (2019).

[12] L. M. Sandratskii, R. F. Egorov, and A. A. Berdyshev, Energy band structure and electronic properties of NiAs type compounds. II. Antiferromagnetic manganese telluride, Phys. Status Solidi B **104**, 103 (1981).

[13] L. Šmejkal, J. Sinova, and T. Jungwirth, Beyond conventional ferromagnetism and antiferromagnetism: A phase with nonrelativistic spin and crystal rotation symmetry, Phys. Rev. X **12**, 031042 (2022).

[14] L. Šmejkal, A. H. MacDonald, J. Sinova, S. Nakatsuji, and T. Jungwirth, Anomalous Hall antiferromagnets, Nat. Rev. Mater. **7**, 482 (2022).

[15] O. Fedchenko, J. Minár, A. Akashdeep, S. W. D'Souza, D. Vasilyev, O. Tkach, L. Odenbreit, Q. Nguyen, D. Kutnyakhov, N. Wind, L. Wenthaus, M. Scholz, K. Rossnagel, M. Hoesch, M. Aeschlimann, B. Stadtmüller, M. Kläui, G. Schönhense, T. Jungwirth, A. B. Hellenes, *et al.*, Observation of time-reversal symmetry breaking in the band structure of altermagnetic RuO_2, Sci. Adv. **10**, eadj4883 (2024).

[16] J. Krempaský, L. Šmejkal, S. W. D'Souza, M. Hajlaoui, G. Springholz, K. Uhlířová, F. Alarab, P. C. Constantinou, V. Strocov, D. Usanov, W. R. Pudelko, R. González-Hernández, A. Birk Hellenes, Z. Jansa, H. Reichlová, Z. Šobáň, R. D. Gonzalez Betancourt, P. Wadley, J. Sinova, *et al.*, Altermagnetic lifting of Kramers spin degeneracy, Nature (London) **626**, 517 (2024).

[17] Y.-P. Zhu, X. Chen, X.-R. Liu, Y. Liu, P. Liu, H. Zha, G. Qu, C. Hong, J. Li, Z. Jiang, X.-M. Ma, Y.-J. Hao, M.-Y. Zhu, W. Liu, M. Zeng, S. Jayaram, M. Lenger, J. Ding, S. Mo, K. Tanaka, *et al.*, Observation of plaid-like spin splitting in a noncoplanar antiferromagnet, Nature (London) **626**, 523 (2024).

[18] K. Samanta, M. Ležaić, M. Merte, F. Freimuth, S. Blügel, and Y. Mokrousov, Crystal Hall and crystal magneto-optical effect in thin films of $SrRuO_3$, J. Appl. Phys. **127**, 213904 (2020).

[19] A. Hariki, Y. Takahashi, and J. Kuneš, X-ray magnetic circular dichroism in RuO_2, Phys. Rev. B **109**, 094413 (2024).

[20] J. Okamoto, R. Wang, Y. Chu, H. Shiu, A. Singh, H. Huang, C. Mou, S. Teh, H. Jeng, K. Du, X. Xu, S. Cheong, C. Du, C. Chen, A. Fujimori, and D. Huang, Giant X-ray circular dichroism in a time-reversal invariant antiferromagnet, Adv. Mater. **36**, 2309172 (2024).

[21] R. González-Hernández, L. Šmejkal, K. Výborný, Y. Yahagi, J. Sinova, T. Jungwirth, and J. Železný, Efficient electrical spin splitter based on nonrelativistic collinear antiferromagnetism, Phys. Rev. Lett. **126**, 127701 (2021).

[22] A. Bose, N. J. Schreiber, R. Jain, D. f. Shao, H. P. Nair, J. Sun, X. S. Zhang, D. A. Muller, E. Y. Tsymbal, D. G.Schlom, and D. C. Ralph, Tilted spin current generated by an antiferromagnet, Nat. Electron. **5**, 263 (2022).

[23] H. Bai, L. Han, X. Y. Feng, Y. J. Zhou, R. X. Su, Q. Wang, L. Y. Liao, W. X. Zhu, X. Z. Chen, F. Pan, X. L. Fan, and C. Song, Observation of spin splitting torque in a collinear antiferromagnet RuO_2, Phys. Rev. Lett. **128**, 197202 (2022).

[24] S. Karube, T. Tanaka, D. Sugawara, N. Kadoguchi, M. Kohda, and J. Nitta, Observation of spin-splitter torque in collinear antiferromagnetic RuO_2, Phys. Rev. Lett. **129**, 137201 (2022).

[25] Y. Guo, J. Zhang, Z. Zhu, Y. Jiang, L. Jiang, C. Wu, J. Dong, X. Xu, W. He, B. He, Z. Huang, L. Du, G. Zhang, K. Wu, X. Han, D. Shao, G. Yu, and H. Wu, Direct and inverse spin splitting effects in altermagnetic RuO_2, Adv. Sci. **11**, 2400967 (2024).

[26] Y. Fan, Q. Wang, W. Wang, D. Wang, Q. Huang, Z. Wang, X. Han, Y. Chen, L. Bai, S. Yan, and Y. Tian, Robust magnetic-field-free perpendicular magnetization switching by manipulating spin polarization direction in RuO_2/[Pt/Co/Pt] heterojunctions, ACS Nano **18**, 26350 (2024).

[27] Z. Li, Z. Zhang, Y. Chen, S. Hu, Y. Ji, Y. Yan, J. Du, Y. Li, L. He, X. Wang, J. Wu, R. Zhang, Y. Xu, and X. Lu, Fully field-free spin-orbit torque switching induced by spin splitting effect in altermagnetic RuO_2, Adv. Mater. **37**, 2416712 (2025).

[28] Y. Zhang, H. Bai, J. Dai, L. Han, C. Chen, S. Liang, Y. Cao, Y. Zhang, Q. Wang, W. Zhu, F. Pan, and C. Song, Electrical manipulation of spin splitting torque in altermagnetic RuO_2, Nat. Commun. **16**, 5646 (2025).

[29] B. Sekh, H. Rahaman, R. Maddu, P. K. Mishra, T. Jin, and S. N. Piramanayagam, Enhanced field-free perpendicular magnetization switching via spin splitting torque in altermagnetic RuO_2-based heterostructures, arXiv:2501.12593.

[30] H. Bai, Y. C. Zhang, Y. J. Zhou, P. Chen, C. H. Wan, L. Han, W. X. Zhu, S. X. Liang, Y. C. Su, X. F. Han, F. Pan, and C. Song, Efficient spin-to-charge conversion via altermagnetic spin splitting effect in antiferromagnet RuO_2, Phys. Rev. Lett. **130**, 216701 (2023).

[31] Y. Liu, H. Bai, Y. Song, Z. Ji, S. Lou, Z. Zhang, C. Song, and Q. Jin, Inverse altermagnetic spin splitting effect-induced terahertz emission in RuO_2, Adv. Opt. Mater. **11**, 2300177 (2023).

[32] X. Feng, H. Bai, X. Fan, M. Guo, Z. Zhang, G. Chai, T. Wang, D. Xue, C. Song, and X. Fan, Incommensurate spin density wave in antiferromagnetic RuO_2 evinced by abnormal spin splitting torque, Phys. Rev. Lett. **132**, 086701 (2024).

[33] C.-T. Liao, Y.-C. Wang, Y.-C. Tien, S.-Y. Huang, and D. Qu, Separation of inverse altermagnetic spin-splitting effect from inverse spin Hall effect in RuO_2, Phys. Rev. Lett. **133**, 056701 (2024).

[34] T. Berlijn, P. C. Snijders, O. Delaire, H.-D. Zhou, T. A. Maier, H.-B. Cao, S.-X. Chi, M. Matsuda, Y. Wang, M. R. Koehler, P. R. C. Kent, and H. H. Weitering, Itinerant antiferromagnetism in RuO_2, Phys. Rev. Lett. **118**, 077201 (2017).

[35] X. Zhou, W. Feng, R.-W. Zhang, L. Smejkal, J. Sinova, Y. Mokrousov, and Y. Yao, Crystal thermal transport in altermagnetic RuO_2, Phys. Rev. Lett. **132**, 056701 (2024).

[36] T. Tschirner, P. Keßler, R. D. Gonzalez Betancourt, T. Kotte, D. Kriegner, B. Büchner, J. Dufouleur, M. Kamp, V. Jovic, L. Smejkal, J. Sinova, R. Claessen, T. Jungwirth, S. Moser, H. Reichlova, and L. Veyrat, Saturation of the anomalous Hall effect at high magnetic fields in altermagnetic RuO_2, APL Mater. **11**, 101103 (2023).

[37] Z. H. Zhu, J. Strempfer, R. R. Rao, C. A. Occhialini, J. Pelliciari, Y. Choi, T. Kawaguchi, H. You, J. F. Mitchell, Y. Shao-Horn, and R. Comin, Anomalous antiferromagnetism in metallic RuO_2 determined by resonant x-ray scattering, Phys. Rev. Lett. **122**, 017202 (2019).

[38] Z. Lin, D. Chen, W. Lu, X. Liang, S. Feng, K. Yamagami, J. Osiecki, M. Leandersson, B. Thiagarajan, J. Liu, C. Felser, and J. Ma, Bulk band structure of RuO_2 measured with soft x-ray angle-resolved photoemission spectroscopy, Phys. Rev. B **111**, 134450 (2025).

[39] A. Smolyanyuk, I. I. Mazin, L. Garcia-Gassull, and R. Valentí, Fragility of the magnetic order in the prototypical altermagnet RuO_2, Phys. Rev. B **109**, 134424 (2024).

[40] P. Keßler, L. Garcia-Gassull, A. Suter, T. Prokscha, Z. Salman, D. Khalyavin, P. Manuel, F. Orlandi, I. I. Mazin, R. Valentí, and S. Moser, Absence of magnetic order in RuO_2: Insights from musr spectroscopy and neutron diffraction, npj Spintronics **2**, 50 (2024).

[41] L. Kiefer, F. Wirth, A. Bertin, P. Becker, L. Bohatý, K. Schmalzl, A. Stunault, J. A. Rodríguez-Velamazan, O. Fabelo, and M. Braden, Crystal structure and absence of magnetic order in single-crystalline RuO_2, J. Phys.: Condens. Matter **37**, 135801 (2025).

[42] J. Liu, J. Zhan, T. Li, J. Liu, S. Cheng, Y. Shi, L. Deng, M. Zhang, C. Li, J. Ding, Q. Jiang, M. Ye, Z. Liu, Z. Jiang, S. Wang, Q. Li, Y. Xie, Y. Wang, S. Qiao, *et al.*, Absence of altermagnetic spin splitting character in rutile oxide RuO_2, Phys. Rev. Lett. **133**, 176401 (2024).

[43] T. Osumi, K. Yamauchi, S. Souma, P. Shubhankar, A. Honma, K. Nakayama, K. Ozawa, M. Kitamura, K. Horiba, H. Kumigashira, C. Bigi, F. Bertran, T. Oguchi, T. Takahashi, Y. Maeno, and T. Sato, Spin-Degenerate bulk bands and topological surface states of RuO_2, arXiv:2501.10649.

[44] M. Hiraishi, H. Okabe, A. Koda, R. Kadono, T. Muroi, D. Hirai, and Z. Hiroi, Nonmagnetic ground state in RuO_2 revealed by muon spin rotation, Phys. Rev. Lett. **132**, 166702 (2024).

[45] M. Wenzel, E. Uykur, S. Rößler, M. Schmidt, O. Janson, A. Tiwari, M. Dressel, and A. A. Tsirlin, Fermi-liquid behavior of nonaltermagnetic RuO_2, Phys. Rev. B **111**, L041115 (2025).

[46] F. Pawula, A. Fakih, R. Daou, S. Hébert, N. Mordvinova, O. Lebedev, D. Pelloquin, and A. Maignan, Multiband transport in RuO_2, Phys. Rev. B **110**, 064432 (2024).

[47] Z. Q. Wang, Z. Q. Li, L. Sun, Z. Y. Zhang, K. He, H. Niu, J. Cheng, M. Yang, X. Yang, G. Chen, Z. Yuan, H. F. Ding, and B. F. Miao, Inverse spin Hall effect dominated spin-charge conversion in (101) and (110)-oriented RuO_2 films, Phys. Rev. Lett. **133**, 046701 (2024).

[48] X. Peng, Z. Liu, S. Zhang, Y. Zhou, Y. Sun, Y. Su, C. Wu, T. Zhou, L. Liu, Y. Li, H. Wang, J. Yang, B. Chen, Y. Li, C. Xi, J. Du, Z. Jiao, Q. Wu, and M. Fang, Universal scaling behavior of transport properties in non-magnetic RuO_2, Commun. Mater. **6**, 177 (2025).

[49] S. Brahimi, D. P. Rai, and S. Lounis, Confinement-induced altermangetism in RuO_2 ultrathin films, J. Phys.: Cond. Mat. **37**, 395801 (2025).

[50] Z. Qian, Y. Yang, S. Liu, and C. Wu, Fragile unconventional magnetism in RuO_2 by proximity to Landau-Pomeranchuk instability, Phys. Rev. B **111**, 174425 (2025).

[51] D. Q. Ho, D. Q. To, R. Hu, G. W. Bryant, and A. Janotti, Symmetry-breaking induced surface magnetization in nonmagnetic RuO_2, Phys. Rev. Mater. **9**, 094406 (2025).

[52] S. G. Jeong, I. H. Choi, S. Nair, L. Buiarelli, B. Pourbahari, J. Y. Oh, N. Bassim, D. Hirai, A. Seo, W. S. Choi, R. M. Fernandes, T. Birol, L. Zhao, J. S. Lee, and B. Jalan, Altermagnetic polar metallic phase in ultra-thin epitaxially-strained RuO_2 films, arXiv:2405.05838.

[53] Z. Yi-Chi, B. Hua, C. Chong, H. Lei, L. Shi-Xuan, C. Rui-Yue, D. Jian-Kun, P. Feng, and S. Cheng, Probing the Néel order in altermagnetic RuO_2 films via x-ray magnetic linear dichroism, Chin. Phys. Lett. **42**, 027301 (2025).

[54] M. Weber, S. Wust, L. Haag, A. Akashdeep, K. Leckron, C. Schmitt, R. Ramos, T. Kikkawa, E. Saitoh, M. Kläui, L. Šmejkal, J. Sinova, M. Aeschlimann, G. Jakob, B. Stadtmüller, and H. C. Schneider, All optical excitation of spin polarization in d-wave altermagnets, arXiv:2408.05187.

[55] S. G. Jeong, S. Lee, B. Lin, Z. Yang, I. H. Choi, J. Y. Oh, S. Song, S. w. Lee, S. Nair, R. Choudhary, J. Parikh, S. Park, W. S. Choi, J. S. Lee, J. M. LeBeau, T. Low, and B. Jalan, Metallicity and anomalous Hall effect in epitaxially strained, atomically thin RuO_2 films, Proc. Natl. Acad. Sci. USA **122**, e2500831122 (2025).

[56] S. Noh, G.-H. Kim, J. Lee, H. Jung, U. Seo, G. So, J. Lee, S. Lee, M. Park, S. Yang, Y. S. Oh, H. Jin, C. Sohn, and J.-W. Yoo, Tunneling magnetoresistance in altermagnetic RuO_2-based magnetic tunnel junctions, Phys. Rev. Lett. **134**, 246703 (2025).

[57] H. Chen, Z. Wang, P. Qin, Z. Meng, X. Zhou, X. Wang, L. Liu, G. Zhao, Z. Duan, T. Zhang, J. Liu, D. Shao, and Z. Liu, Altermagnetic spin-splitting magnetoresistance, Adv. Mater. **37**, 2507764 (2025).

[58] C. M. Schneider, M. S. Hammond, P. Schuster, A. Cebollada, R. Miranda, and J. Kirschner, Observation of magnetic circular dichroism in uv photoemission from ferromagnetic fcc cobalt films, Phys. Rev. B **44**, 12066 (1991).

[59] J. Bansmann, C. Westphal, M. Getzlaff, F. Fegel, and G. Schönhense, Magnetic circular dichroism in valence-band photo-emission from Fe(100), J. Magn. Magn. Mater. **104-107**, 1691 (1992).

[60] J. Stöhr, Y. Wu, B. D. Hermsmeier, M. G. Samant, G. R. Harp, S. Koranda, D. Dunham, and B. P. Tonner, Element-Specific magnetic microscopy with circularly polarized x-rays, Science **259**, 658 (1993).

[61] G. van der Laan and B. T. Thole, Spin polarization and magnetic dichroism in photoemission from core and valence states in localized magnetic systems. II. Emission from open shells, Phys. Rev. B **48**, 210 (1993).

[62] J. Braun, The theory of angle-resolved ultraviolet photoemission and its applications to ordered materials, Rep. Prog. Phys. **59**, 1267 (1996).

[63] H. Ebert and J. Schwitalla, Magnetic dichroism in valence-band x-ray photoemission spectroscopy, Phys. Rev. B **55**, 3100 (1997).

[64] J. Henk, T. Scheunemann, S. V. Halilov, and R. Feder, Magnetic dichroism and electron spin polarization in photoemission: Analytical results, J. Phys.: Condens. Matter **8**, 47 (1996).

[65] T. Yokoyama, T. Nakagawa, and Y. Takagi, Magnetic circular dichroism for surface and thin film magnetism: Measurement techniques and surface chemical applications, Int. Rev. Phys. Chem. **27**, 449 (2008).

[66] K. Hild, J. Maul, G. Schönhense, H. J. Elmers, M. Amft, and P. M. Oppeneer, Magnetic circular dichroism in two-photon photoemission, Phys. Rev. Lett. **102**, 057207 (2009).

[67] G. Schönhense, Circular dichroism and spin polarization in photoemission from adsorbates and non-magnetic solids, Phys. Scr. **T31**, 255 (1990).

[68] S. Beaulieu, J. Schusser, S. Dong, M. Schüler, T. Pincelli, M. Dendzik, J. Maklar, A. Neef, H. Ebert, K. Hricovini, M. Wolf, J. Braun, L. Rettig, J. Minár, and R. Ernstorfer, Revealing hidden orbital pseudospin texture with time-reversal dichroism in photoelectron angular distributions, Phys. Rev. Lett. **125**, 216404 (2020).

[69] M. Schüler, T. Pincelli, S. Dong, T. P. Devereaux, M. Wolf, L. Rettig, R. Ernstorfer, and S. Beaulieu, Polarization-Modulated angle-resolved photoemission spectroscopy: Toward circular dichroism without circular photons and Bloch wave-function reconstruction, Phys. Rev. X **12**, 011019 (2022).

[70] H. Ueda, Y. Tanaka, Y. Wakabayashi, and T. Kimura, Observation of collinear antiferromagnetic domains making use of the circular dichroic charge-magnetic interference effect of resonant x-ray diffraction, Phys. Rev. B **98**, 134415 (2018).

[71] S. Sakamoto, T. Higo, M. Shiga, K. Amemiya, S. Nakatsuji, and S. Miwa, Observation of spontaneous x-ray magnetic circular dichroism in a chiral antiferromagnet, Phys. Rev. B **104**, 134431 (2021).

[72] H. Ikeno, F. M. F. de Groot, E. Stavitski, and I. Tanaka, Multiplet calculations of $L_{2,3}$ x-ray absorption near-edge structures for 3d transition-metal compounds, J. Phys.: Condens. Matter **21**, 104208 (2009).

[73] E. Stavitski and F. M. de Groot, The CTM4XAS program for EELS and XAS spectral shape analysis of transition metal l edges, Micron **41**, 687 (2010).

[74] L. Šmejkal, J. Sinova, and T. Jungwirth, Emerging research landscape of altermagnetism, Phys. Rev. X **12**, 040501 (2022).

[75] V. Jovic, R. J. Koch, S. K. Panda, H. Berger, P. Bugnon, A. Magrez, K. E. Smith, S. Biermann, C. Jozwiak, A. Bostwick, E. Rotenberg, and S. Moser, Dirac nodal lines and flat-band surface state in the functional oxide RuO_2, Phys. Rev. B **98**, 241101(R) (2018).

[76] Z. Feng, X. Zhou, L. Šmejkal, L. Wu, Z. Zhu, H. Guo, R. González-Hernández, X. Wang, H. Yan, P. Qin, X. Zhang, H. Wu, H. Chen, Z. Meng, L. Liu, Z. Xia, J. Sinova, T. Jungwirth, and Z. Liu, An anomalous Hall effect in altermagnetic ruthenium dioxide, Nat. Electron. **5**, 735 (2022).

[77] M. Kallmayer, K. Hild, T. Eichhorn, H. Schneider, G. Jakob, A. Conca, M. Jourdan, H. J. Elmers, A. Gloskovskii, S. Schuppler, and P. Nagel, Solid state reaction at the interface between Heusler alloys and AL cap accelerated by elevated temperature and rough surface, Appl. Phys. Lett. **91**, 192501 (2007).

[78] See Supplemental Material at http://link.aps.org/supplemental/10.1103/x2h4-rtky for additional experimental results measured by photoemission electron microscopy (PEEM) on films with different thicknesses.

[79] S. Babenkov, K. Medjanik, D. Vasilyev, S. Chernov, C. Schlueter, A. Gloskovskii, Y. Matveyev, W. Drube, B. Schönhense, K. Rossnagel, H.-J. Elmers, and G. Schönhense, High-accuracy bulk electronic bandmapping with eliminated diffraction effects using hard x-ray photoelectron momentum microscopy, Commun. Phys. **2**, 107 (2019).

[80] K. Medjanik, S. V. Babenkov, S. Chernov, D. Vasilyev, B. Schönhense, C. Schlueter, A. Gloskovskii, Y. Matveyev, W. Drube, H. J. Elmers, and G. Schönhense, Progress in HAXPES performance combining full-field k-imaging with time-of-flight recording, J. Synchrotron Radiat. **26**, 1996 (2019).

[81] L. Šmejkal, R. González-Hernández, T. Jungwirth, and J. Sinova, Crystal time-reversal symmetry breaking and spontaneous Hall effect in collinear antiferromagnets, Sci. Adv. **6**, eaaz8809 (2020).

[82] T. Noll and F. Radu, The mechanics of the Vekmag experiment, in *Proceedings of the 9th Edition of the Mechanical Engineering Design of Synchrotron Radiation Equipment and Instrumentation Conference, MEDSI'2016, Spain* (JACoW Publishing, Geneva, Switzerland, 2017), pp. 370–373.

[83] A. Winkelmann, B. Schröter, and W. Richter, Simulation of high energy photoelectron diffraction using many-beam dynamical Kikuchi-band theory, Phys. Rev. B **69**, 245417 (2004).

[84] O. Fedchenko, A. Winkelmann, S. Chernov, K. Medjanik, S. Babenkov, S. Y. Agustsson, D. Vasilyev, M. Hoesch, H.-J. Elmers, and G. Schönhense, Emitter-site specificity of hard x-ray photoelectron Kikuchi-diffraction, New J. Phys. **22**, 103002 (2020).

[85] T.-P. Vo, O. Tkach, S. Tricot, D. Sébilleau, J. Braun, A. Pulkkinen, A. Winkelmann, O. Fedchenko, Y. Lytvynenko, D. Vasilyev, H.-J. Elmers, G. Schönhense, and J. Minár, Layered multiple scattering approach to hard x-ray photoelectron diffraction: Theory and application, npj Comput. Mater. **11**, 159 (2025).

[86] L. Baumgarten, C. M. Schneider, H. Petersen, F. Schäfers, and J. Kirschner, Magnetic x-ray dichroism in core-level photoemission from ferromagnets, Phys. Rev. Lett. **65**, 492 (1990).

[87] J. P. Ruf, H. Paik, N. J. Schreiber, H. P. Nair, L. Miao, J. K. Kawasaki, J. N. Nelson, B. D. Faeth, Y. Lee, B. H. Goodge, B. Pamuk, C. J. Fennie, L. F. Kourkoutis, D. G. Schlom, and K. M. Shen, Strain-stabilized superconductivity, Nat. Commun. **12**, 59 (2021).

[88] R. D. Cowan, *The Theory of Atomic Structure and Spectra* (University of California Press, Oakland, CA, 1981).

[89] Z. Hu, H. von Lips, M. S. Golden, J. Fink, G. Kaindl, F. M. F. de Groot, S. Ebbinghaus, and A. Reller, Multiplet effects in the Ru $L_{2,3}$ x-ray-absorption spectra of Ru(IV) and Ru(V) compounds, Phys. Rev. B **61**, 5262 (2000).

[90] F. d. Groot, Multiplet effects in x-ray spectroscopy, Coord. Chem. Rev. **249**, 31 (2005).

[91] F. M. de Groot, H. Elnaggar, F. Frati, R.-p. Wang, M. U. Delgado-Jaime, M. van Veenendaal, J. Fernandez-Rodriguez, M. W. Haverkort, R. J. Green, G. van der Laan, Y. Kvashnin, A. Hariki, H. Ikeno, H. Ramanantoanina, C. Daul, B. Delley, M. Odelius, M. Lundberg, O. Kuhn, S. I. Bokarev, *et al.*, 2p x-ray absorption spectroscopy of 3d transition metal systems, J. Electron Spectrosc. Relat. Phenom. **249**, 147061 (2021).

[92] B. Z. Gregory, J. Strempfer, D. Weinstock, J. P. Ruf, Y. Sun, H. Nair, N. J. Schreiber, D. G. Schlom, K. M. Shen, and A. Singer, Strain-induced orbital-energy shift in antiferromagnetic RuO_2 revealed by resonant elastic x-ray scattering, Phys. Rev. B **106**, 195135 (2022).

[93] C. A. Occhialini, V. Bisogni, H. You, A. Barbour, I. Jarrige, J. F. Mitchell, R. Comin, and J. Pelliciari, Local electronic structure of rutile RuO_2, Phys. Rev. Res. **3**, 033214 (2021).

[94] N. Sasabe, M. Mizumaki, T. Uozumi, and Y. Yamasaki, Ferroic order for anisotropic magnetic dipole term in collinear antiferromagnets of $(t_{2g})^4$ system, Phys. Rev. Lett. **131**, 216501 (2023).